The onset of CVD graphene formation on γ-Al_2O_3 is promoted by unsaturated CH_2 end

Qi Zhao[a], Masanori Yamamoto[b], , Kaoru Yamazaki[c†], Hirotomo Nishihara[b], Rachel Crespo-Otero[a]*, Devis Di Tommaso[a]*

[a] Department of Chemistry, Queen Mary University of London, Mile End Road, London E1 4NS, UK
[b] Advanced Institute for Materials Research (WPI-AIMR) / Institute of Multidisciplinary Research for Advanced Materials, Tohoku University, 2−1−1 Katahira, Aoba, Sendai 980−8577, Japan
[c] Institute for Materials Research, Tohoku University, 2-1-1 Katahira, Aoba, Sendai 980-8577, Japan
[†]Present Address: RIKEN Center for Advanced Photonics, RIKEN, 2-1 Hirosawa, Wako, Saitama 351–0198, Japan

Corresponding Authors: r.crespo-otero@qmul.ac.uk, d.ditomaso@qmul.ac.uk

Abstract

Chemical vapor deposition of methane onto a template of alumina (Al_2O_3) nanoparticles is a prominent synthetic strategy of graphene meso-sponge, a new class of nanoporous carbon materials consisting of single-layer graphene walls. However, the elementary steps controlling the early stages of graphene growth on Al_2O_3 surfaces are still not well understood. In this study, density functional calculations provide insights into the initial stages of graphene growth. We have modelled the mechanism of CH_4 dissociation on (111), (110), (100), and (001) γ-Al_2O_3 surfaces. Subsequently, we have considered the reaction pathway leading to the formation of a C6 ring. We found the γ-Al_2O_3(110) and γ-Al_2O_3(100) are both active for CH_4 dissociation, but the (100) surface has a higher catalytic activity towards the carbon growth reaction. The overall mechanism involves the formation of the reactive intermediate CH_2* that then can couple to form C_nH_{2n}* (n = 2-6) species. The unsaturated CH_2 end promotes the sustained carbon growth in a nearly barrierless process. Also, the short length between terminal carbon atoms leads to strong interactions, which might lead to the high activity among unsaturated CH_2* of hydrocarbon chain. Analysis of the electron localization and geometries of the carbon chains reveal the formation of C-Al-σ bonds with the chain growing towards the gas rather than C-Al-π bonds covering the γ-Al_2O_3(100) surface. This growth behaviour prevents catalysis poison during the initial stage of graphene nucleation.

Key Words: CH_4, carbon growth, graphene, γ-Al_2O_3, density functional calculations

1. Introduction

Graphene, the atomic thick layer of carbon, has been called a ‘wonder material’ due to its superior properties such as its high charge carrier mobility, high optical transmissivity, high tensile strength, and excellent thermal conductivity[1-4]. Geim and Novoselov first produced graphene by using mechanical exfoliation technique with Scotch tape®, which provides high

quality graphene, i.e., monolayer and defect-free[1]. However, this method is only applicable to small-area production. A variety of methods have then been developed to produce large-area and high-quality graphene including chemical exfoliation[1], electrochemical exfoliation[5, 6], chemical synthesis[7, 8], and chemical vapor deposition (CVD)[9, 10]. Among these techniques, CVD is one of the most promising synthetic methods because it can produce monolayer graphene over a large area[7, 8, 11-14].

Various hydrocarbon feedstocks have been successfully used as carbon sources, ranging from gases such as methane (CH_4)[3, 15, 16] and ethylene[17], liquids such as benzene[18], to solids such as polymethylmethacrylate (PMMA)[19] and amorphous carbon thin films[20, 21]. Since it can generate single-layered graphene (SLG), the most popular combination of carbon feedstock and substrate for graphene production is CH_4 and Cu[22]. In addition to Cu, different metal substrates, including Ni[14, 23-26] , Ru[27-29], Ir[30-32], Co[33, 34], Fe[35], Au[36], Rh[37], Pt[38, 39], and their alloys[40, 41], have been used for CVD synthesis of graphene films. Also, graphene layers can directly grow on insulating substrates such as SiC[41, 42], sapphire[43], SiO_2[44, 45], and h-BN[46, 47] .

Recently, oxides of earth abundant catalysts without noble metal supporting like MgO[48], CaO[49] and Al_2O_3[50] have been reported as substrates in the synthesis of novel graphene meso-sponge (GMS), a new class of mesoporous carbon materials consisting mainly of single-layer graphene walls with an unique set of properties compared to traditional graphene materials: higher surface area, more developed mesopores, higher oxidation resistance[51, 52], higher softness and elasticity, lower bulk modulus, and better force-driven reversible liquid–gas phase transition[53]. Hence, a better understanding of the reaction mechanisms is required to modify the catalytic sites and make them more active in the processes involved. These processes include CH_4 activation, formation of carbon-hydrogen nuclei, and the subsequent edge growth of graphene islands. By combining experiments and density functional theory (DFT), we previously found that oxygen vacancies on the metal oxide surface of γ-Al_2O_3[54, 55] play an influential role on the CH_4* activation. For further graphene growth study, Park et al.[55] have reported calculations of graphene nucleation mechanism on γ-Al_2O_3, but in their work, the hypothesis was that growth occurs from adsorbed C* atoms. Alister J. Page et al.[56] have also reported graphene nucleation on γ-Al_2O_3 using a simplified surface model that did not consider hydroxylated surfaces, which we recently demonstrated to remain during realistic experimental conditions[54].

In this work, we focus on the initial stages of graphene nucleation on hydroxylated atomistic models of γ-Al_2O_3(110) and γ-Al_2O_3(100) using DFT calculations, transition-state modelling, and electron localization function analysis. In addition to the complete dehydrogenation of

CH_4* to C* and subsequent sequential formation of graphene nuclei, we found the methylene (CH_2*) coupling path to be the lowest energy pathway to the growth of graphene. Our calculations indicate that the radical CH_2* is involved in the CH_4 conversion into various C_nH_{2n}* (n = 2-6) intermediates during the formation of graphene on γ-Al_2O_3(100) in the CVD processes. We also found that the CH_4* activation and nucleation occur preferentially on the γ-Al_2O_3(100) surface rather than γ-Al_2O_3(110).

2. Computational details

DFT calculations were performed by using the "Vienna *ab initio* simulation package" (VASP.5.4.1). We used the Perdew–Burke–Ernzerhof (PBE) generalized-gradient approximation (GGA) for the exchange and correlation terms[57], under a spin-polarized model and the Grimme's-D3 dispersion correction[58], which provides a more accurate description of the ionic induce dipole interaction than standard DFT-GGA methods[59]. A plane-wave basis set was employed within the framework of the projector augmented wave method[60]. Transition states (TSs) for the elementary reactions were located using the climbing image nudged elastic band (CI-NEB) method[61]. The convergence criteria for both TS searching and single point calculation were 0.05 eV $Å^{-1}$. We used a Monkhorst-Pack k-point grid of (3×3×1) and the plane-wave cut-off was 450 eV. All atoms were relaxed during the structural optimization of γ-Al_2O_3 and reaction intermediates.

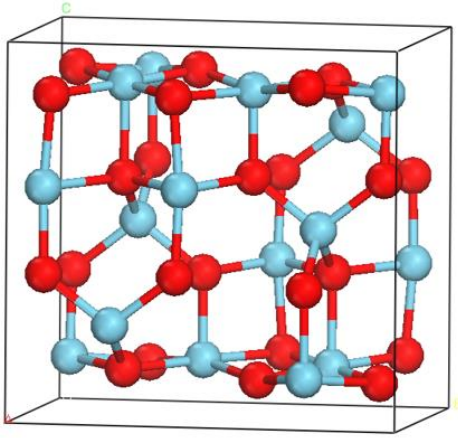

Al: tetrahedral

Al: octahedral

Crystallographic structure of bulk γ-alumina

Space group	P21/m	experimental value
a (Ă)	5.538	5.587
b (Ă)	8.347	8.413
c (Ă)	8.024	8.068
β (°)	90.603	90.59
Atom	Position	(x, y, z)

Figure 1. The bulk cell of γ-Al_2O_3 (red and blue sphere represent the O anions and Al cations respectively). Parameters of optimized γ-Al_2O_3 bulk and experiment value are listed in the table [62].

IR experiments showed that isolated hydroxyl groups (around 3701 cm^{-1}) at the γ-Al_2O_3 surfaces are present even after annealing at 900 ºC for 30 min[54]. Starting from the optimized bulk structure with the parameters shown in **Fig. 1**, we built a p(1×1) slab of partially hydrated γ-Al_2O_3 (100) surface containing 4 atomic layers of the oxide and 15 Å vacuum. The

mechanisms of CH_4 activation and carbon nucleation were also investigated using the OH-covered γ-Al_2O_3 (111), γ-Al_2O_3 (110) and γ-Al_2O_3 (001) surfaces. These models are shown in **Fig. 2**. Herein we have mainly modelled the reactions assuming the tetrahedrally-coordinated (4-coordinated) Al as the active site because we have previously shown that these Al centers to be the most favorable towards the CH_4 activation[54]. The adsorption energies were computed using the following expression:

$$E_{\text{ads}} = E(\text{adsorbate} + \text{slab}) - E(\text{adsorbate}) - E(\text{slab}) \quad (1)$$

where the first term is the energy of the optimized surface slab with the adsorbate, the second term is the energy of the isolated optimized adsorbate molecule, and the third term is the energy of the optimized bare surface slab. Negative values of E_{ads} correspond to an exothermic adsorption process.

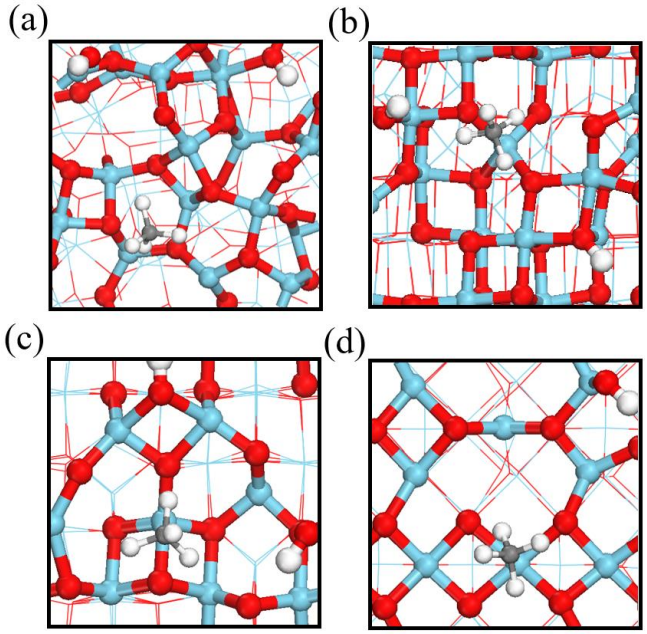

Figure 2. Top view of CH_4* adsorption models on (a) γ-Al_2O_3(111); (b) γ-Al_2O_3(110); (c) γ-Al_2O_3(100); (d) γ-Al_2O_3(001). (Red, blue, gray, and white spheres represent the O, Al, C and H atoms respectively).

3. Results and Discussion

3.1 Methane activation on γ-Al_2O_3

We report the calculations of the intermediates and transition states of the first two steps of the CH_4* dehydrogenation, CH_4* → CH_3* + H* and CH_3* + H* → CH_2* + 2H*. The profiles in **Fig. 3(b)** show the ability to activate CH_4* depending on the surface of γ-Al_2O: (100), (110), (111), and (001). The structures of the intermediates and transitions states on the γ-Al_2O_3 (100) surface are reported in **Fig. 3(a)**. For the other surfaces, these structures are shown in **Fig. S2** of Supporting Information.

On γ-Al_2O_3 (100), the exothermic adsorption of CH_4* (E_{ads} =–0.20 eV) is followed by the breakage of the first C–H bond with a barrier of 1.20 eV and a reaction energy of 0.10 eV. The subsequent dehydrogenation of CH_3* has a barrier of 1.32 eV and reaction energy of –0.06 eV. The barriers for the dissociate step CH_4* → CH_3* + H* on the (111), (001), and (110) are 1.92 eV, 1.46 eV, and 1.66 eV, respectively (**Fig. 3(b)**). The subsequent dehydrogenation step, CH_3* → CH_2* + H*, requires even higher barriers. Consequently, the first two CH_4* dehydrogenation steps are kinetically favorable on the γ-Al_2O_3 (100) surface. Martínez et al. reported that CH_2* leads to spontaneous C–C chain growth[63]. Hence, the ability to promote the CH_3* dehydrogenation step to generate a stable CH_2* species will also assess the catalytic activity towards carbon growth. However, stable CH_2* will be a trapped species on (111) surface due to unfavorable thermodynamic and kinetic conversion energies depicted in the blue line of **Fig. 3(b).** These calculations indicate the (100) and (110) surfaces as the most catalytically active for CH_4* activation. We have considered these γ-Al_2O_3 surfaces to investigate the subsequent steps of CH_2* coupling that initiates the graphene growth. Note that the (111) surface is more unstable than the (100) and (110) surfaces[64] and the (111) surface nearly does not contribute to the CH_4 activation.

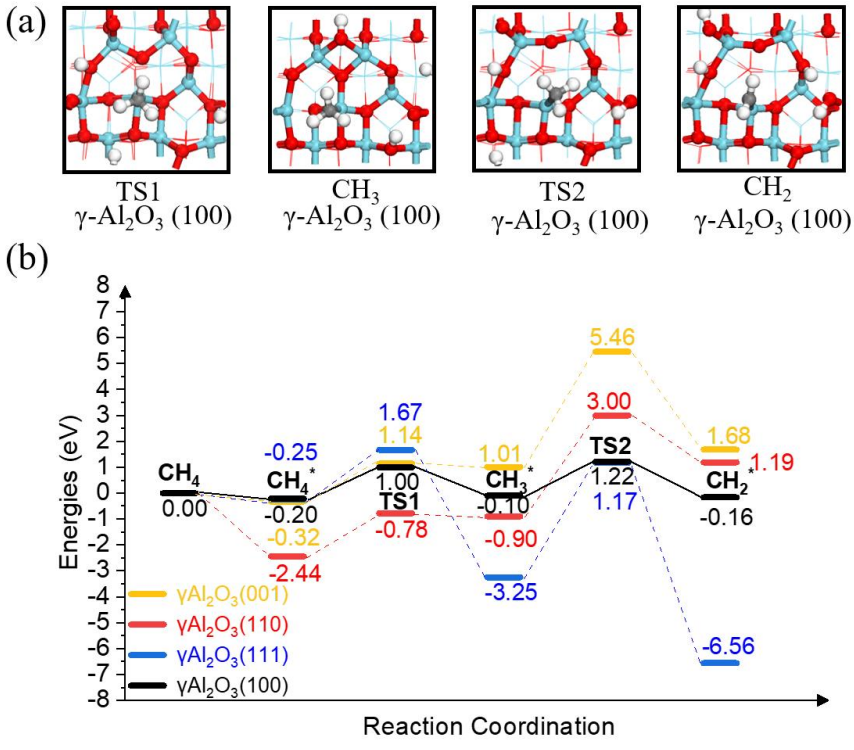

Figure 3. (a) The structures of intermediates and translation states of the first two CH_4* dehydrogenation steps on the γ-Al_2O_3 (100) surface. (Red, blue, gray, and white spheres represent the O, Al, C, and H, respectively); **(b)** The energy profiles of the first two steps of the CH_4* dehydrogenation, CH_4* → CH_3* + H* and CH_3* → CH_2* + H*, on the γ-Al_2O_3 (001), γ-Al_2O_3 (111), γ-Al_2O_3 (110) and γ-Al_2O_3 (100) surfaces.

The CH_4 molecules interacts significantly with the Al_2O_3 (110) surface with an adsorption energy of –2.44 eV (**Fig. 3(b)**). According to the volcano-type relationship between activity and bond strength illustrated in the Sabatier principle[65], the strong adsorbed CH_4 would tightly bound on γ-Al_2O_3 (110) hindering the next step of the reaction. On the other hand, Park *et al.*[55, 66] and Cholewinski *et al.*[55, 66] reported that γ-Al_2O_3 (110) can have different levels of hydroxyl coverages that in turn could affect the strength of CH_4* interaction with the surface. To resolve this contradiction, we have considered several models of γ-Al_2O_3 (110) with varying OH coverage, from 2.4 OH/nm^2 (2OH; one H_2O molecule per supercell) to 9.8 OH/nm^2 (8OH, four H_2O molecules per supercell). These models are shown in **Fig. S3** of Supporting Information. As shown in **Fig. S1**, the activation barriers of the first CH_4 dehydrogenation step on the 6OH and 8OH models are twice the ones of 2OH and 4OH. For the subsequent dehydrogenation step, the high barrier on the 4OH model also suggests no catalytic activation of the C–H bond on this surface. Consequently, the catalysis of the C–H breaking can only occur for low OH coverage of γ-Al_2O_3 (110).

3.2 Contribution of the (100) and (110) surfaces on the CH_2 generation

Here, we evaluate the contributions of the (100) and (110) surfaces on the CH_4 activation in terms of methane activation rate constant *k*. CH_2 generation on the γ-Al_2O_3 surface is a pseudo-first order reaction on the methane partial pressure [54]. If the entropy contribution is negligible, *k* can be approximated with an Eyring-like equation as a function of reaction temperature *T*,

$$k(T) \sim \frac{k_B T}{h} \exp\left[-\frac{E^*}{k_B T}\right], \quad (2)$$

where k_B and *h* are the Boltzmann and Planck constants, and E^* represents effective activation energy which experimentally measurable via Arrhenius plot[67]. For the (100) surface, the CH_4 is weakly physiosorbed on the surface (E_{ads} (CH_4^*) = -0.20 eV) and E^* can be calculated as the energy difference between E_{ads} (TS2) and E_{ads} (CH_4). For (110), the CH_4 is strongly physiosorbed on the surface (E_{ads} (CH_4^*) = -2.44 eV) and the E^* can be obtained as the difference between E_{ads} (TS2) and E_{ads} (CH_4^*)[67]. The effective activation energies and rate constants at T = 900 ℃ are summarized in Table 1. The value of E^* = 1.22 eV for (100) reasonably agrees with the experimental one (1.29 eV). The obtained value of k(T = 900 ℃) is 1.40 x 10^8 s^{-1} .For (110) with 2 OH groups, the value of E^* = 4.78 eV is too large and consequently the rate is negligibly small (k(T = 900 ℃) = 7.14 x 10^{-8} s^{-1}). These calculations indicate that the generation of CH_2 mostly occurs on the (100) surface. The hydroxylated surface can generate CH_3 as shown in Figure S1, however subsequent dehydrogenation is kinetically unfavorable. Hereafter, we focus on the reactions on the (100) surface.

Table 1. Calculated effective activation energies (E^*) for the generation of CH_2 and rate constants $k(T)$ at T = 900 ℃ obtained using Eq. 2. a) This rate constant was estimated using the experimental barrier.

Surface	***E**** **(eV)**	***k*** **(s^{-1})**
(100)	1.22	1.40×10^{8}
(110) 2OH	4.78	7.14×10^{-8}
Experiment[54]	1.29	7.01×10^{7a}

3.3 Onset of graphene formation: methylene coupling and carbon chain growth

We then investigated a complete dehydrogenation of CH_4 on the γ-Al_2O_3 (100) surface as a representative surface leading to the formation of an adsorbed carbon atom. The complete dehydrogenation of CH_4 on the γ-Al_2O_3 (100) surface leads to the formation of an adsorbed carbon atom. **Fig. 4(a)** shows that while the first two dehydrogenation steps $CH_4^* \rightarrow CH_3^* + H^*$ and $CH_3^* + H^* \rightarrow CH_2^* + 2H^*$ are both favourable, the subsequent steps $CH_2^* + 2H^* \rightarrow CH^* + 3H^*$ and $CH^* + 3H^* \rightarrow C^* + 4H^*$ are endothermic with high activation barriers. Therefore, the CH_2^* species could be a key intermediate during the CVD growth of graphene on the γ-Al_2O_3 (100) surface. But since the pyrolytic carbon deposition of CH_4 occurs at temperatures higher than 800°C[54], CH_4 could be dissociated into CH_3^*, CH_2^*, CH* and C* species on the catalytic surface. To verify the relative stability of these species, we have compared in **Fig. 4(b)** the binding energies (E_b) of the CH_n (n = 0–4) on γ-Al_2O_3 (100). For CH_4^*, CH_3^*, and CH_2^*, the value of E_b is between 0.2 and 0.62 and 0.49 eV, but for CH* and C* are 4.3 and 4.1 eV, respectively. According to the Sabatier principle, the strong binding of CH* and C* on γ-Al_2O_3 (100) may poison the active centres. We may conclude that the CVD growth of graphene on alumina does not involve CH* and C* species. Therefore, we hypothesize the next steps in the formation of C–C bonds on the γ-Al_2O_3 (100) surface are the coupling reactions $2CH_3^* \rightarrow C_2H_6^*$ (**Fig. 4(c)**) and $2CH_2^* \rightarrow C_2H_4^*$ (**Fig. 4(d)**). The pathway leading to $C_2H_4^*$ in **Fig. 4(d)** has a lower activation barrier (0.19 eV) compared to $C_3H_6^*$ (0.82 eV) shown in **Fig. 4(c)**. Moreover, the subsequent coupling of CH_3^* with the $C_2H_6^*$ intermediate is unlikely to occur as the CH_3 ends of the molecule is saturated, inhibiting further growth as shown in **Fig. S4** and **Fig. S5** of Supporting Information. We have also calculated that the dehydrogenation of $C_2H_6^*$ into $C_2H_4^*$ is unlikely to occur as this reaction is both kinetically hindered (E_a = 4.5 eV) and thermodynamically unfavourable (ΔE= 1.7 eV) as shown

in **Fig. S6**. From the above results, we can conclude that C_2H_4* generated by the CH_2* coupling reaction is the key intermediate for the subsequent carbon growth steps.

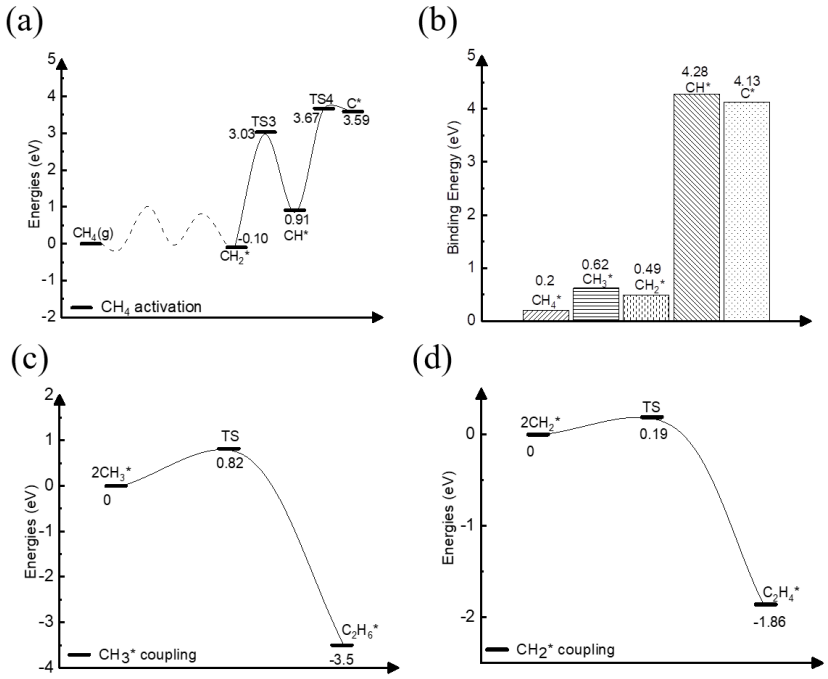

Figure 4. Energy profiles of the CH_4* dissociation, CH_x* (x = 0–4) binding, and CH_y* (y = 2, 3) coupling reaction on the γ-Al_2O_3 (100) surface. **(a)** Complete CH_4* dehydrogenation; **(b)** Binding energies of CH_4*, CH_3*, CH_2*, CH* and C; **(c)** CH_3* coupling; **(d)** CH_2* coupling. The asterisk (*) denotes a molecule adsorbed on the γ-Al_2O_3 (100) surface.

Starting from C_2H_4*, we have computed the methylene coupling processes to form linear C_nH_{2n}* (n = 3–6) species and the C_6H_{12} ring unit, the minimal unit of graphene on γ-Al_2O_3 (100). The energy profile of the chain growth reactions and the corresponding snapshots are shown in **Fig. 5 and 6**, respectively. **Fig. 5** shows that like the CH_2* to C_2H_4* coupling reaction, the subsequent methylene coupling processes have low activation barriers and are thermodynamically favorable with each adsorption step, C_nH_{2n} + CH_2(g) → C_nH_{2n} + CH_2*, having favorable reaction energies in the order of –2 eV. The barrier of formation of C_2H_4*, C_3H_6*, C_5H_{10}*, C_6H_{12}* and the C6 ring are all well below 1 eV. The exception is the step CH_2* + C_3H_6* →C_4H_8* with an activation energy of 1.87 eV, whose explanation will be shown in the next section. In addition to coupling with another surface CH_2* unit to achieve carbon chain growth, both unsaturated CH_2* ends are also active to couple with each other to form a carbon ring shown in **Fig. S7**. This reaction undergoes the barrier of 0.34 eV and the reaction energy of –3.09 eV. These results confirm that the role of unsaturated CH_2* end during the graphene nucleation stage which makes the initial growth process to be highly favorable.

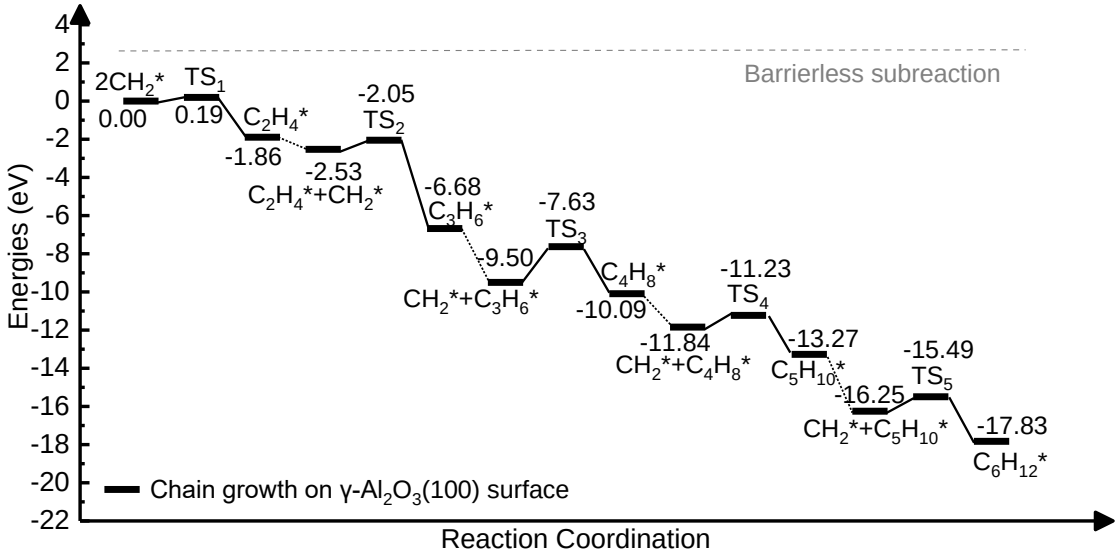

Figure 5. Energy profile of the formation of C_nH_{2n}* (n = 2-6) species via CH_2* coupling on the γ-Al_2O_3 (100) surface.

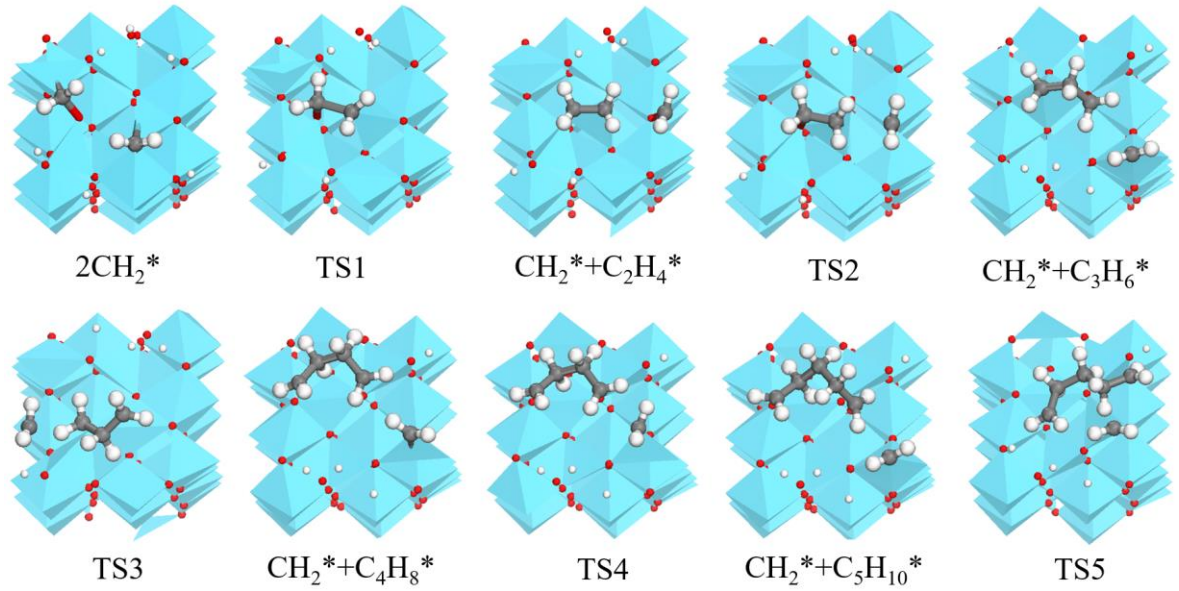

Figure 6. Structures of the formation of C_nH_{2n}* (n = 2-6) species via CH_2* coupling on the γ-Al_2O_3 (100) surface.

3.4 The role of unsaturated CH_2 end in promoting graphene growth

To understand the process of CH_2* coupling leading to the carbon chain growth on the γ-Al_2O_3 (100) surface, we have computed the electron localization function (ELF) of the linear C_nH_{2n} (n = 2–6) intermediates. The ELF maps in **Fig. 7** represent the electron cloud localized and delocalized around atoms. Using this information, we can determine critical points, chemical bonds, and regions relevant for reactivity (red and orange) (**Fig. 8**).

The ELF map for the C_2H_4* structure in **Fig. 7(b)** shows a localized electron around one end of CH_2* (red area) and a lower electronic charge density distribution around the other end. This weakly saturated CH_2* end allows coupling with free CH_2* on the γ-Al_2O_3 (100) surface making the formation of C_2H_4* highly favorable (**Fig.5**). When the longer carbon chains C_4H_8*, C_5H_{10}* and C_6H_{12}* are formed, the sole CH_2* end of C_nH_{2n}* is located on the γ-Al_2O_3 (100) surface as shown in **Figs. 7(d)-(f)**. Consequently, the initial growth direction of carbon occurs away from the surface and the long carbon species form C-Al-σ bond with γ-Al_2O_3 (100) surface rather than grow along the catalytic surface forming C-Al-π bond. Otherwise, the accumulation of C_nH_{2n}* species on the surface would poison the catalyst in the very early stage by covering these heavy carbon species on the surface, which protect CVD graphene nucleation reaction sites on γ-Al_2O_3 (100) to remain active. This 'loop' away surface carbon growth mechanism previously proposed by Zhu *et al.*[68] in the case of Ni clusters.

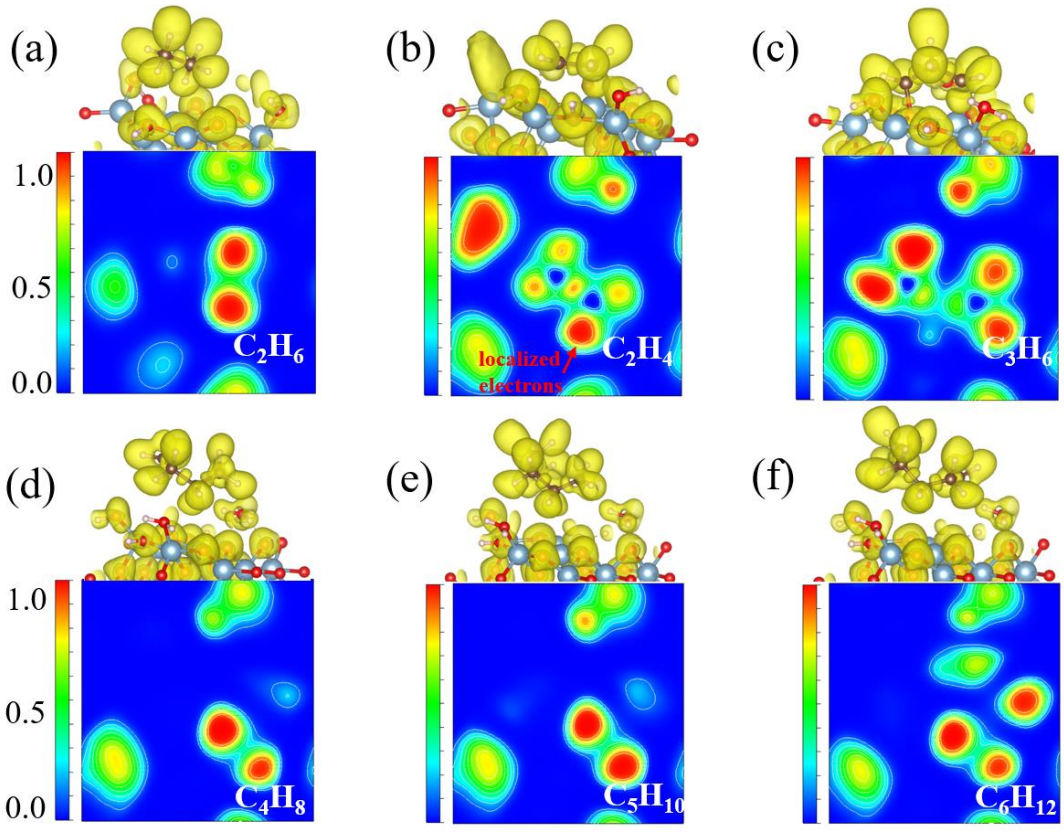

Figure 7. The electron localization function maps and corresponding side view structures with localized electrons of **(a)** C_2H_6*; **(b)** C_2H_4*; **(c)** C_3H_6*; **(d)** C_4H_8*; **(e)** C_5H_{10}*; **(f)** C_6H_{12}*. Ongoing from the blue to the red area, there is an increase in electron density, i.e., red areas indicate electron localization.

We can use the ELF analysis to rationalize the high activation energy (1.87 eV**)** of the CH_2* + C_3H_6* coupling step shown in **Fig. 5**. The ELF map of C_3H_6* (**Fig. 7(c))** shows that the electron density of both ends of CH_2* in C_3H_6* are highly localized on the catalyst

surface because the C atoms of the methylene groups are both coordinated to the sites on the alumina surface. This situation leads to a high barrier for the CH_2* + C_3H_6*→ C_4H_8* step (**Fig. 5)** as the CH_2* ends are both saturated**.** Unsaturated CH_2* species play, therefore, a crucial role in promoting the nucleation reaction on γ-Al_2O_3.

The length of the C–C bonds of the C_nH_{2n} species binding on γ-Al_2O_3(100) expands with the chain length (**Fig. 8**), which could support the carbon units growing away from the Al_2O_3(100) surface with the formation of C-Al-σ bonds rather than C-Al-π bonds covering the surface[63]. In addition, from **Fig. 8**, the C-C length between carbon atoms close to the solid surface is longer than the C-C length of carbon atoms away from the surface. For instance, the structure of C_6H_{12}* in **Fig. 8(g)** shows that for the C atoms in the middle positions, C1, C2, C3 and C4, the distances are d(C1-C2) = 1.54 Å, d(C1-C3) = 1.54 Å, d(C2-C4) = 1.54 Å. In comparison, for the terminal C atoms, C5 and C6, d(C4-C6) = 1.49 Å and d(C3-C5) = 1.49 Å. A similar situation can be found in C_4H_8* and C_5H_{10}*. Shorter bond lengths between terminal carbons correspond to stronger interatomic interaction, which might contribute to the high activity among unsaturated CH_2* of the hydrocarbon chain.

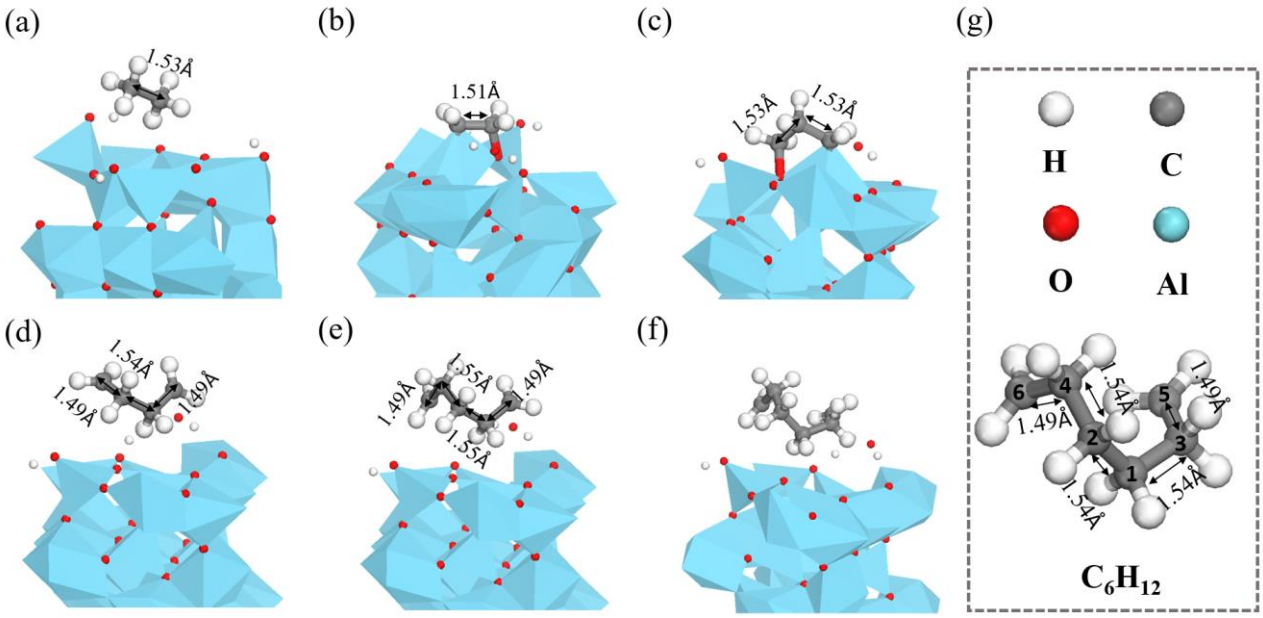

Figure 8 The structures of **(a)** C_2H_6*, **(b)** C_2H_4*, **(c)** C_3H_6*, **(d)** C_4H_8*, **(e)** C_5H_{10}*, **(f)** C_6H_{12}* on γ-Al_2O_3(100) and **(g)** bond length in C_6H_{12} structure.

3.5 Dehydrogenation of C_nH_{2n} species

We have demonstrated that the methylene coupling reaction on γ-Al_2O_3 leading to C_nH_{2n} species is favorable compared to complete CH_4* dehydrogenation (**Figs. 3-4**). Consequently, according to our simulations the species involved in the early stage of graphene growth will contain hydrogen. A possible picture is that small carbon-containing species are not stable without H until they grow to a defined size. **Figure. 9** shows the dehydrogenation ability of hydrocarbon chains. The intermediates C_3H_6*, C_4H_8*, C_5H_{10}* and C_6H_{12}* will not lose hydrogen due to the demanding activation barrier and the significantly endothermic energies. Xie et al. have reported that similar sequential PT on a Lewis acid/base pair will also activate intermediate hydrocarbons including propane to give unsaturated hydrocarbons and hydrogen with a comparable barrier of C-H activation[69]. Even after the formation of C6 ring, it is still hard to desorb H from the hydrocarbon species depicted in **Fig. S8**. However, in the early nucleation stage, H transfer among carbon atoms is much easier than H desorption from carbon (**Fig. S9**).

These results indicate that the initial steps of graphene growth involve carbon species that contain hydrogens and confirm that the process does not involve the formation of single carbon. These hydrogens could also hinder the formation of a strong binding carbon island covering the catalyst surface. With this picture, an interesting question is when hydrogen-free graphene flake would nucleate. In perspective, we look forward to answering this question with our future work and filling the gap between hydrogen-free graphene nucleation and the hydrocarbon sub-intermediates in the nucleation stage.

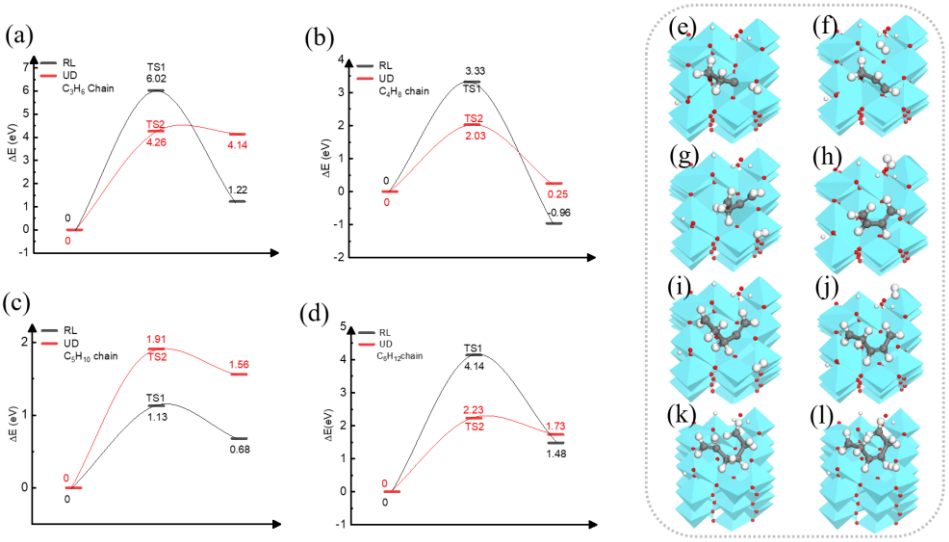

Figure 9. The energy profiles for the dehydrogenation of carbon chains to form H_2 gas **(a)** C_3H_6*; **(b)** C_4H_8*; **(c)** C_5H_{10}* and **(d)** C_6H_{12}*. The structures of **(e), (f)** C_3H_6* UD and RL desorption; **(g), (h)** C_4H_8* UD and RL desorption, **(i), (j)** C_5H_{10}* UD and RL desorption, **(k), (l)** C_6H_{12}* UD and RL desorption. on γ-Al_2O_3(100). (Red spheres represent the O atoms; blue spheres represent the Al atoms; gray spheres represent the C atoms; white spheres represent the hydrogen atoms). The asterisk (*) denotes a molecule adsorbed on the Al_2O_3(100) surface.

RL: two H atoms on the right and left neighbour carbons to form H_2; UD: two H atoms on the up and down same carbon to form H_2.

Conclusions

We have reported a systematic investigation of the mechanism of CH_4* dissociation and formation of C_nH_{2n} (n = 2–6) species on γ-Al_2O_3. We found the (100) to be the most active for the CH_4* dissociation compared with other low-index surfaces of γ-Al_2O_3. On this surface, the methylene coupling to C_2H_4* is kinetically and thermodynamically more favourable than the complete CH_4* dehydrogenation to form C. Starting from C_2H_4*, we have modelled the formation of linear C_nH_{2n}* (n = 3–6) species and the C_6H_{12} ring unit, which is the minimal graphene unit. We found these early stages of graphene nucleation are nearly barrierless. ELF and structural analysis of carbon chains reveal that the early stages of nucleation involve the formation of C–Al σ bonds with chains "looping" away from the catalysis surface and unsaturated CH_2* end remaining active. This is favorable for the initial steps of graphene growth. Our calculations show that hydrogenated carbon species are involved in the early stages of graphene nucleation. These protective bonded hydrogens could weaken the direct C-Al interaction, which could remain active sites for heavy carbon covering the γ-Al_2O_3 (100) surface. In this work, our calculations illustrate the first steps of graphene nucleation on γ-Al_2O_3 surfaces and give insight into the role of different active species during the catalytic process

Supplementary Material

See the supplementary material for the energy diagram of the first two CH_4 dehydrogenation steps on γ-Al_2O_3 (110) with different OH coverages (Figure S1), the structures in intermediates and translation states in the first two steps of the CH_4 dehydrogenation on γ-Al_2O_3 surfaces (Figure S2), structures of γ-Al_2O_3 (110) with different OH coverage (Figure S3); NEB searching for C_2H_6 interacting with surface flexible carbon species (Figure S4) and NEB intermediates structures for C_2H_6 interacting with surface flexible carbon species (Figure S5); energy diagram and structures of the C_2H_6 dehydrogenation (Figure S6); energy diagram and structures of C_6H_{12} ring formation process (Figure S7); energy diagram and structures of C_6H_{12} ring desorption (Figure S8); energy diagram and structures for H-transfer and H desorption after carbon ring (Figure S9).

Acknowledgement

This work was supported by Cooperative Research Program for CORE lab of "Five-star Alliance", JST SICORP Grant no. JPMJSC2112, Ensemble Grant for Early Career Researchers at Tohoku University, and the UK's Royal Society International Exchanges Cost Share (IEC\R3\193106). Q.Z. thanks the China Scholarship Council for financial support. K.Y. is grateful for the financial support from Building of Consortia for the Development of Human Resources in Science and Technology funded by MEXT and Core Research for Evolutional Science and Technology of the Japan Science and Technology Agency (JST CREST, Grant No. JPMJCR16P3). We are grateful to the UK Materials and Molecular Model-ling Hub for computational resources, which is partially funded by EPSRC (EP/P020194/1). Via our membership of the UK's HEC Materials Chemistry Consortium, which is funded by EPSRC (EP/L000202), this work used the ARCHER UK National Supercomputing Service (http://www.archer.ac.uk). This research utilized Queen Mary's Apocrita HPC facility, supported by QMUL Research-IT. http://doi.org/10.5281/zenodo.438045.

Reference

1. K. S. Novoselov, A. K. Geim, S. V. Morozov, D.-e. Jiang, Y. Zhang, S. V. Dubonos, I. V. Grigorieva and A. A. Firsov, *Science*, 2004, **306**, 666-669.
2. A. A. Balandin, *Nature Materials*, 2011, **10**, 569-581.
3. A. A. Balandin, *Nature Nanotechnology*, 2010, **5**, 574-578.
4. C. Lee, X. Wei, J. W. Kysar and J. Hone, *Science*, 2008, **321**, 385-388.
5. P. Yu, S. E. Lowe, G. P. Simon and Y. L. Zhong, *Current Opinion in Colloid & Interface Science*, 2015, **20**, 329-338.
6. J. Liu, Springer Singapore, 2017.
7. S. Eigler, M. Enzelberger-Heim, S. Grimm, P. Hofmann, W. Kroener, A. Geworski, C. Dotzer, M. Röckert, J. Xiao and C. Papp, *Advanced Materials*, 2013, **25**, 3583-3587.
8. S. Stankovich, D. A. Dikin, R. D. Piner, K. A. Kohlhaas, A. Kleinhammes, Y. Jia, Y. Wu, S. T. Nguyen and R. S. Ruoff, *Carbon*, 2007, **45**, 1558-1565.
9. A. Reina, S. Thiele, X. Jia, S. Bhaviripudi, M. S. Dresselhaus, J. A. Schaefer and J. Kong, *Nano Res*, 2009, **2**, 509-516.
10. X. Li, W. Cai, L. Colombo and R. S. Ruoff, *ACS Nano Letters*, 2009, **9**, 4268-4272.
11. K. Parvez, S. Yang, X. Feng and K. Müllen, *Synthetic Metals*, 2015, **210**, 123-132.
12. Y. Zhang, L. Zhang and C. Zhou, *ACCOUNTS OF CHEMICAL RESEARCH*, 2013, **46**, 2329-2339.
13. M. A. Azam, N. N. Zulkapli, N. Dorah, R. N. A. R. Seman, M. H. Ani, M. S. Sirat, E. Ismail, F. B. Fauzi, M. A. Mohamed, B. Y. Majlis, *ECS Journal of Solid State Science and Technology*, 2017, **6**, M3035-M3048.
14. A. Reina, X. Jia, J. Ho, D. Nezich, H. Son, V. Bulovic, M. S. Dresselhaus and J. Kong, *ACS NANO LETTERS*, 2009, **9**, 30-35.
15. X. Li, W. Cai, J. An, S. Kim, J. Nah, D. Yang, R. Piner, A. Velamakanni, I. Jung and E. Tutuc, *SCIENCE*, 2009, **324**, 1312-1314.
16. J. K. Wassei, M. Mecklenburg, J. A. Torres, J. D. Fowler, B. Regan, R. B. Kaner and B. H. Weiller, *SMALL*, 2012, **8**, 1415-1422.
17. L. Gao, J. R. Guest and N. P. Guisinger, *ACS Nano Letters*, 2010, **10**, 3512-3516.
18. Z. Li, P. Wu, C. Wang, X. Fan, W. Zhang, X. Zhai, C. Zeng, Z. Li, J. Yang and J. Hou, *ACS Nano*, 2011, **5**, 3385-3390.
19. Z. Sun, Z. Yan, J. Yao, E. Beitler, Y. Zhu and J. M. Tour, *Nature* 2010, **468**, 549-552.

20. T. Liang, Y. Kong, H. Chen and M. Xu, *Chin. J. Chem*, 2016, **34**, 32-40.
21. H. Ji, Y. Hao, Y. Ren, M. Charlton, W. H. Lee, Q. Wu, H. Li, Y. Zhu, Y. Wu and R. Piner, *ACS Nano*, 2011, **5**, 7656-7661.
22. P. Wu, W. Zhang, Z. Li and J. L. Yang, *Small*, 2014, **10**, 2136-2150.
23. M. Xu, D. Fujita, K. Sagisaka, E. Watanabe and N. Hanagata, *ACS Nano*, 2011, **5**, 1522-1528.
24. Q. Yu, J. Lian, S. Siriponglert, H. Li, Y. P. Chen and S.-S. Pei, *Appl. Phys. Lett.* , 2008, **93**, 113103.
25. K. S. Kim, Y. Zhao, H. Jang, S. Y. Lee, J. M. Kim, K. S. Kim, J.-H. Ahn, P. Kim, J.-Y. Choi and B. H. Hong, *Nature*, 2009, **457**, 706-710.
26. J. Lahiri, T. Miller, L. Adamska, I. I. Oleynik and M. Batzill, *ACS Nano Letters*, 2011, **11**, 518-522.
27. P. W. Sutter, J.-I. Flege and E. A. Sutter, *Nature Materials*, 2008, **7**, 406-411.
28. E. Loginova, N. C. Bartelt, P. J. Feibelman and K. F. McCarty, *New Journal of Physics*, 2008, **10**, 093026.
29. E. Loginova, N. Bartelt, P. Feibelman and K. F. McCarty, *New Journal of Physics*, 2009, **11**, 063046.
30. E. Loginova, S. Nie, K. Thürmer, N. C. Bartelt and K. F. McCarty, *PHYSICAL REVIEW B*, 2009, **80**, 085430.
31. J. Coraux, M. Engler, C. Busse, D. Wall, N. Buckanie, F.-J. M. Zu Heringdorf, R. Van Gastel, B. Poelsema and T. Michely, *New Journal of Physics*, 2009, **11**, 023006.
32. P. Lacovig, M. Pozzo, D. Alfe, P. Vilmercati, A. Baraldi and S. Lizzit, *Phys. Rev. Lett.*, 2009, **103**, 166101.
33. O. Rader, A. Varykhalov, J. Sánchez-Barriga, D. Marchenko, A. Rybkin and A. M. Shikin, *PhysRevLett.*, 2009, **102**, 057602.
34. D. Eom, D. Prezzi, K. T. Rim, H. Zhou, M. Lefenfeld, S. Xiao, C. Nuckolls, M. S. Hybertsen, T. F. Heinz and G. W. Flynn, *Nano Letters*, 2009, **9**, 2844-2848.
35. N. A. Vinogradov, A. A. Zakharov, V. Kocevski, J. Rusz, K. A. Simonov, O. Eriksson, A. Mikkelsen, E. Lundgren, A. S. Vinogradov, N. Mårtensson and A. B. Preobrajenski, *Physical Review Letters*, 2012, **109**, 026101.
36. S. Nie, N. C. Bartelt, J. M. Wofford, O. D. Dubon, K. F. McCarty and K. Thürmer, *Physical Review B*, 2012, **85**, 205406.
37. E. N. Voloshina, Y. S. Dedkov, S. Torbrügge, A. Thissen and M. Fonin, *Appl. Phys. Lett.*, 2012, **100**, 241606.
38. P. Sutter, J. T. Sadowski and E. Sutter, *Physical Review B*, 2009, **80**, 245411.
39. X. Feng, J. Wu, A. T. Bell and M. Salmeron, *The Journal of Physical Chemistry C*, 2015, **119**, 7124-7129.
40. X. Liu, L. Fu, N. Liu, T. Gao, Y. Zhang, L. Liao and Z. Liu, *The Journal of Physical Chemistry C*, 2011, **115**, 11976-11982.
41. T. Wu, X. Zhang, Q. Yuan, J. Xue, G. Lu, Z. Liu, H. Wang, H. Wang, F. Ding, Q. Yu, X. Xie and M. Jiang, *Nature Materials*, 2016, **15**, 43-47.
42. C. Riedl, C. Coletti, T. Iwasaki, A. A. Zakharov and U. Starke, *Physical Review Letters*, 2009, **103**, 246804.
43. M. K. Jeonghyun Hwang, Dorr Campbell, Hussain A. Alsalman, Joon Young Kwak, Shriram Shivaraman, Arthur R. Woll, Arunima K. Singh, Richard G. Hennig, Sandeep Gorantla, Mark H. Rümmeli, and Michael G. Spencer, *ACS Nano*, 2013, **7**, 385-395.
44. J. Chen, Y. Wen, Y. Guo, B. Wu, L. Huang, Y. Xue, D. Geng, D. Wang, G. Yu and Y. Liu, *Journal of the American Chemical Society*, 2011, **133**, 17548-17551.
45. H. Bi, S. Sun, F. Huang, X. Xie and M. Jiang, *Journal of Materials Chemistry*, 2012, **22**, 411-416.
46. J. Xue, J. Sanchez-Yamagishi, D. Bulmash, P. Jacquod, A. Deshpande, K. Watanabe, T. Taniguchi, P. Jarillo-Herrero and B. J. LeRoy, *Nature Materials*, 2011, **10**, 282-285.
47. W. Yang, G. Chen, Z. Shi, C.-C. Liu, L. Zhang, G. Xie, M. Cheng, D. Wang, R. Yang, D. Shi, K. Watanabe, T. Taniguchi, Y. Yao, Y. Zhang and G. Zhang, *Nature Materials*, 2013, **12**, 792-797.
48. S. Sunahiro, K. Nomura, S. Goto, K. Kanamaru, R. Tang, M. Yamamoto, T. Yoshii, J. N. Kondo, Q. Zhao, A. Ghulam Nabi, R. Crespo-Otero, D. Di Tommaso, T. Kyotani and H. Nishihara, *Journal of Materials Chemistry A*, 2021, **9**, 14296-14308.
49. C. Tang, B. Q. Li, Q. Zhang, L. Zhu, H. F. Wang, J. L. Shi and F. Wei, *Adv. Funct. Mater.*, 2016, **26**, 577-585.

50. H. Nishihara, T. Simura, S. Kobayashi, K. Nomura, R. Berenguer, M. Ito, M. Uchimura, H. Iden, K. Arihara, A. Ohma, Y. Hayasaka and T. Kyotani, *Adv. Funct.Mater.*, 2016, **26**, 6418-6427.
51. M. Yamamoto, S. Goto, R. Tang, K. Nomura, Y. Hayasaka, Y. Yoshioka, M. Ito, M. Morooka, H. Nishihara, T. Kyotani, ACS Appl. Mater. Interfaces, 2021, **13**, 38613-38622.
52. K. Nomura, H. Nishihara, N. Kobayashi, T. Asada, T. Kyotani and E. Science, 2019, **12**, 1542-1549.
53. K. Nomura, H. Nishihara, M. Yamamoto, A. Gabe, M. Ito, M. Uchimura, Y. Nishina, H. Tanaka, M. T. Miyahara and T. Kyotani, *Nature Communications*, 2019, **10**, 2559.
54. M. Yamamoto, Q. Zhao, S. Goto, Y. Gu, T. Toriyama, T. Yamamoto, H. Nishihara, A. Aziz, R. Crespo-Otero and D. Di Tommaso, *Chemical Science*, 2022, **13**, 3140-3146.
55. J. Park, J. Lee, J.-H. Choi, D. K. Hwang and Y. W. Song, *Scientific Reports*, 2015, **5**, 11839.
56. A. J. Page, S. Saha, H.-B. Li, S. Irle and K. J. Morokuma, *J. Am. Chem. Soc.*, 2015, **137**, 9281-9288.
57. J. P. Perdew, K. Burke and M. Ernzerhof, *Physical Review Letters*, 1996, **77**, 3865-3868.
58. S. Grimme, J. Antony, S. Ehrlich and H. Krieg, *J Chem Phys*, 2010, **132**, 154104.
59. P. E. Blöchl, *Physical Review B*, 1994, **50**, 17953-17979.
60. G. Kresse and D. Joubert, *Physical Review B*, 1999, **59**, 1758-1775.
61. J. Paier, R. Hirschl, M. Marsman and G. Kresse, *J Chem Phys*, 2005, **122**, 234102.
62. X. Krokidis, P. Raybaud, A.-E. Gobichon, B. Rebours, P. Euzen and H. Toulhoat, *The Journal of Physical Chemistry B*, 2001, **105**, 5121-5130.
63. L. Martínez, P. Merino, G. Santoro, J. I. Martínez, S. Katsanoulis, J. Ault, Á. Mayoral, L. Vázquez, M. Accolla, A. Dazzi, J. Mathurin, F. Borondics, E. Blázquez-Blázquez, N. Shauloff, R. Lebrón-Aguilar, J. E. Quintanilla-López, R. Jelinek, J. Cernicharo, H. A. Stone, V. A. de la Peña O'Shea, P. L. de Andres, G. Haller, G. J. Ellis and J. A. Martín-Gago, *Nature Communications*, 2021, **12**, 5937.
64. M. Digne, *Journal of Catalysis*, 2004, **226**, 54-68.
65. A. J. Medford, A. Vojvodic, J. S. Hummelshøj, J. Voss, F. Abild-Pedersen, F. Studt, T. Bligaard, A. Nilsson and J. K. Nørskov, *Journal of Catalysis*, 2015, **328**, 36-42.
66. M. C. Cholewinski, M. Dixit and G. Mpourmpakis, *ACS Omega*, 2018, **3**, 18242-18250.
67. W. Grünert, *Journal*, 2012.
68. W. Zhu, A. Börjesson and K. Bolton, *Carbon*, 2010, **48**, 470-478.
69. Z. Xie, Z. Li, P. Tang, Y. Song, Z. Zhao, L. Kong, X. Fan and X. Xiao, *Journal of Catalysis*, 2021, **397**, 172-182.